energies

Article

Toward Reducing Undesired Rotation Torque in Maglev Permanent Magnet Synchronous Linear Motor

Feng Xing [1], Xiaoyu Song [1], Yuge Gao [2] and Chaoning Zhang [3,*]

1 School of Electrical Engineering, Liaoning University of Technology, Jinzhou 121001, China
2 School of Electrical Engineering and Automation, Harbin Institute of Technology, Harbin 150001, China
3 Department of Artificial Intelligence, Kyung Hee University, Seoul 02447, Republic of Korea
* Correspondence: chaoningzhang1990@gmail.com; Tel.: +82-10-7104-0708

Abstract: The *dq* current transformation method can be used to achieve the drive control of the maglev permanent magnet synchronous linear motor (MPMSLM). Specifically, the control of the suspension force F_z can be achieved by controlling the *d*-axis current, and the control of the thrust force F_x can be achieved by controlling the *q*-axis current. However, the direct use of the *dq* current transformation method on traditional MPMSLM structures produces an additional rotation torque around the *y*-axis. In order to reduce this additional torque, a new MPMSLM structure is proposed in this work. First, the characteristics of additional torque through finite element analysis are analyzed. Second, the Halbach permanent magnet array and coil size are optimized, and the topology of the MPMSLM coil is designed to reduce the additional torque. The decoupling performance and current of the proposed MPMSLM are experimentally verified through open-loop experiments using finite element simulation software. Finally, the decoupling algorithm of the generalized inverse matrix is used to achieve the decoupling between forces F_x and F_z and torque T_y and the *d*-axis and *q*-axis currents in each drive unit. Based on this, a three-degree-of-freedom closed-loop control system of the MPMSLM is designed. The LabVIEW 2018 software is used for the simulation analysis of the three-degree-of-freedom MPMSLM motion control system, and the results show that the proposed motor structure has superior closed-loop control performance.

Keywords: *dq* current transformation; MPMSLM; additional torque; three degrees of freedom

Citation: Xing, F.; Song, X.; Gao, Y.; Zhang, C. Toward Reducing Undesired Rotation Torque in Maglev Permanent Magnet Synchronous Linear Motor. *Energies* **2023**, *16*, 6066. https://doi.org/10.3390/en16166066

Academic Editor: Frede Blaabjerg

Received: 29 June 2023
Revised: 11 August 2023
Accepted: 15 August 2023
Published: 19 August 2023

1. Introduction

Linear motors have become an interesting solution for linear positioning applications. Compared with the traditional approach of using rotating motors and mechanical structures for linear motion control, the structure of directly driving linear motors has a more compact mechanical structure and is more suitable for the high dynamic performance requirements of motion control. Linear motors have been widely applied in various fields, such as transportation [1,2], high-precision positioning platforms [3,4], and electromagnetic launch systems [5,6], etc.

There are typically three types of support and guidance for linear motion mechanisms: mechanical [7,8], air bearing [9,10], and magnetic levitation [11–13]. The mechanical method is widely used in linear motor structures due to its low cost and simple technology. However, it is limited by the fact that friction between mechanical components cannot be completely eliminated and the mechanical parts might also wear out due to physical contact. Air bearing is a common non-contact support method where there is no mechanical friction between the mover and stator, and there is no need for lubrication which thus avoids dust and oil pollution. However, there are some remaining issues, such as high-pressure gas causing high-frequency vibration of the suspension components, low gas-supported stiffness, and weak load bearing and shock resistance. Some high-precision equipment and production processes require a vacuum environment, which limits the application of air bearing. Using magnetic levitation not only eliminates mechanical friction but also has high stiffness. When designing the center of gravity of moving components, a lower center of gravity is more suitable for high-acceleration and high-precision motion control. In [14], the authors proposed a novel magnetically levitated linear stage driven by linear hysteresis motors. The platform achieves levitation control in three degrees of freedom using passive magnetic levitation support. By adopting the magnetic levitation support structure, the number of actuators and sensors required is reduced, resulting in a more compact platform design. In [15], a system comprising four two-degrees-of-freedom moving magnet linear motors was developed to create magnetically levitated positioners. This system is applied in motion control scenarios requiring high positioning accuracy with multiple degrees of freedom. Moreover, the use of magnetic levitation in linear motors planar motors enables direct operation in a vacuum environment [16], which has attracted widespread attention from scholars.

To achieve decoupled control of the magnetic levitation linear motor and planar motor, the wrench–current decoupling method is applied in the multi-degree-of-freedom control of the linear motor and planar motor. In [17], the authors investigated a long-stroke magnetically levitated linear actuator. This actuator utilizes permanent magnets as the moving part, which introduces the need to consider not only decoupling in the control process but also the issue of coil switching. Handling the coil switching is crucial for the proper functioning of the actuator. The authors of [18] proposed a magnetically levitated planar motor that utilizes high-temperature super-conductor coils. This planar motor is designed to achieve multi-degree-of-freedom motion control, and it employs a control strategy where each coil requires individual power supply to function effectively. The above decoupling control strategy is that each coil adopts an H-bridge driving unit composed of four switching devices for power supply, and the three-phase winding requires twelve switching devices in total. When the ABC three-phase current allocation is implemented using the *dq* transformation method, it can be implemented on a driving unit consisting of six switching devices, which saves half of the switching devices compared with the wrench–current decoupling method. However, when the *dq* control strategy is used for force control, it can bring about an additional rotation torque. In [19], the authors address the issue of generating additional torque in an iron core linear permanent magnet motor using *dq*-decomposition. They achieve this by fitting the harmonic model of finite element results and measurement data, thereby modeling the torque component as a function of the motor position. To control the torque at any position, the required *d*-axis and *q*-axis currents are determined from the torque model. However, this method does not reduce the torque generated at its source and requires a more complex decoupling design.

Traditional *dq* current transformation can transform an ABC three-phase current into a *d*-axis current and *q*-axis current. Control over the horizontal force F_x and the suspension force F_z can be achieved by controlling the currents i_q and i_d [20]. However, both F_x and F_z are forces composed of three sets of forces generated by the windings, and these three forces are a function relative to the magnetic field position. Although the amplitude of the superimposed forces on the *x*-axis and the *z*-axis is constant, an additional yet undesired rotation torque will be generated. In the linear motor structure with mechanical support, the air gap change between the linear motor movers is limited by the guide rail and slider. In the maglev permanent magnet synchronous linear motor (MPMSLM) motion control process, three degrees of freedom need to be controlled, namely horizontal movement along the *x*-axis, suspension movement along the *z*-axis, and rotation around the *y*-axis. In the magnetic levitation support structure, due to the absence of mechanical constraints, this additional torque will directly act on the mover, causing the air gap to change and leading to poor control. Therefore, to achieve motion control in three degrees of freedom, it is necessary to generate controllable torque for mitigating this additional rotation.

In order to reduce the additional torque generated when using the *dq* transformation method, a new MPMSLM structure is proposed in reference [21], as shown in Figure 1. The stator of the MPMSLM is composed of a Halbach permanent magnet array, and the mover is composed of two sets of three-phase windings. In Figure 1, the MPMSLM consists of motor units I and II. Each motor unit consists of a set of three-phase windings, and the winding corresponding to each unit is 4.5τ phase-shifted from the other unit. Motor unit I consist of coils A_1, B_1, and C_1 and is powered by one set of drivers. Motor unit II also consists of coils A_2, B_2, and C_2 and is powered by a separate set of drivers. In this way, the additional torque generated by the two sets of windings due to the *d*-axis current is almost the same in magnitude but opposite in direction, and the superposition has a smaller fluctuation magnitude.

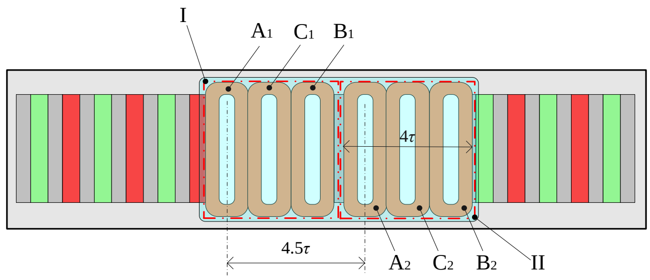

Figure 1. The motor structure proposed in literature [21].

In order to further improve the high control performance of the MPMSLM, this work proposes a new motor structure after optimizing the additional torque. The main difference between the structure of the magnetically levitated permanent magnet synchronous linear motor proposed in this paper and the one shown in Figure 1 lies in the coil topology of the mover. This motor introduces two sets of three-phase windings. Therefore, in the magnetically levitated permanent magnet synchronous linear motor proposed in this paper, there are two sets of three-phase windings on the left and right sides of the mover. On the left side of the mover, the two sets of three-phase windings (A, B, and C phase coils) are connected in series. The same connection method is applied on the right side of the mover. This configuration enables each side of the mover to be powered by a single driving unit, simplifying the power supply system for the motor. The structure has smaller torque fluctuation and a longer equivalent lever arm in the horizontal direction, which can reduce the required current of the driving unit.

This work is organized as follows. Section 2 analyzes the causes of additional torque and the variables affecting torque through finite element modeling and establishes an analytical model of the electromagnetic force. In Section 3, a new MPMSLM structure is optimized to reduce the additional torque. Firstly, the parameters of the Halbach permanent magnet array are simulated and designed, followed by the simulation design of the coil thickness, and finally, the simulation and comparative analysis of the topology of the primary coil is carried out based on the previous designs. In Section 4, the motion control system of the new MPMSLM structure is designed, and the closed-loop control performance is analyzed. This includes the design of decoupling algorithms, the design of the closed-loop control system structure, and the establishment of a three-degree-of-freedom control system using LabVIEW 2018 software for closed-loop simulation analysis. A brief conclusion is provided in Section 5.

2. Torque Analysis

2.1. Finite Element Simulation Analysis

The MPMSLM has three degrees of freedom: horizontal motion along the *x*-axis, levitation along the *z*-axis, and rotation around the *y*-axis. With the three-phase current transformed into the *dq* domain, the control of the levitation force can be achieved by controlling the *d*-axis current, and the control of the horizontal thrust can be achieved by controlling the *q*-axis current. However, an additional torque is also generated, which causes an undesirable rotation around *y*-axis. Therefore, how to keep the rotation around the *y*-axis within a small range during motion control is still an open question.

In order to analyze the forces and torques generated in the ABC three-phase windings under d-axis current excitation and q-axis current excitation, an ANSYS Electronics finite element model was created for analysis. In the transient field simulation, the ABC three-phase windings were moved along the horizontal direction at a speed of 1.5 m/s, while maintaining an air gap height of 1 mm during the motion process.

Figure 2 shows the curves of the suspension forces and the total suspension force generated by the three-phase windings of a motor unit when only the d-axis current is applied. In Figure 2, the suspension forces generated by the three sets of windings, A, B, and C, are represented as $F_{z\mathrm{A}}$, $F_{z\mathrm{B}}$, and $F_{z\mathrm{C}}$, respectively. It can be observed that the forces generated by each set of windings are sinusoidal functions relative to the magnetic field position but with different phases. The total suspension force $F_{z\mathrm{ABC}}$ generated by the motor unit is the sum of forces $F_{z\mathrm{A}}$, $F_{z\mathrm{B}}$, and $F_{z\mathrm{C}}$. It can be seen that force $F_{z\mathrm{ABC}}$ remains constant during the linear motor movement. The magnitude of force $F_{z\mathrm{ABC}}$ can be controlled by controlling the magnitude of the d-axis current, From the above analysis, it can be concluded that the electromagnetic forces generated by the three-phase windings can be directly added to obtain a constant suspension force. However, the torque is the product of the force generated by each set of windings and its lever arm. Since the lever arms from the three sets of windings to the center of the moving part are different, a torque fluctuation occurs with position.

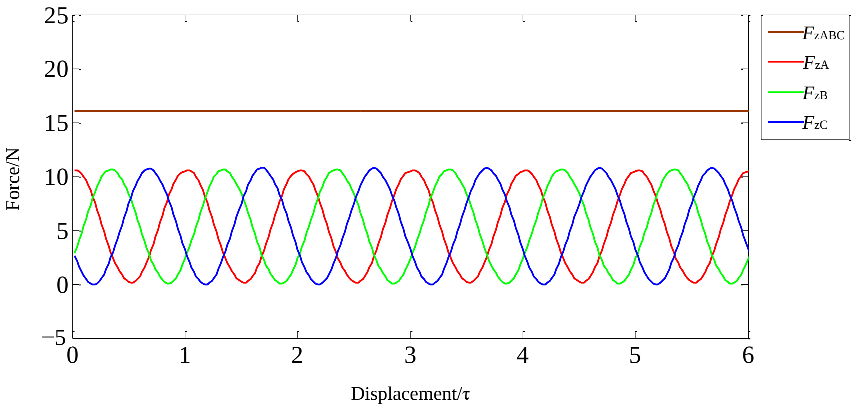

Figure 2. Suspension force under d-axis current excitation (finite element simulation).

The curves of the suspension forces and the total horizontal force generated by the three-phase windings of a motor unit when only the q-axis current is applied are shown in Figure 3. It can be observed that controlling the q-axis current allows for the control of horizontal force $F_{x\mathrm{ABC}}$, which is the sum of the horizontal forces generated by the three-phase windings. When the q-axis current is applied, each phase winding also produces a force along the z-axis, represented as $F_{z\mathrm{A}}$, $F_{z\mathrm{B}}$, and $F_{z\mathrm{C}}$. The characteristic of these forces is that the sum of the three-phase forces is zero. This is also due to the different lever arms from the three sets of windings to the center of the moving part, resulting in a torque fluctuation with position.

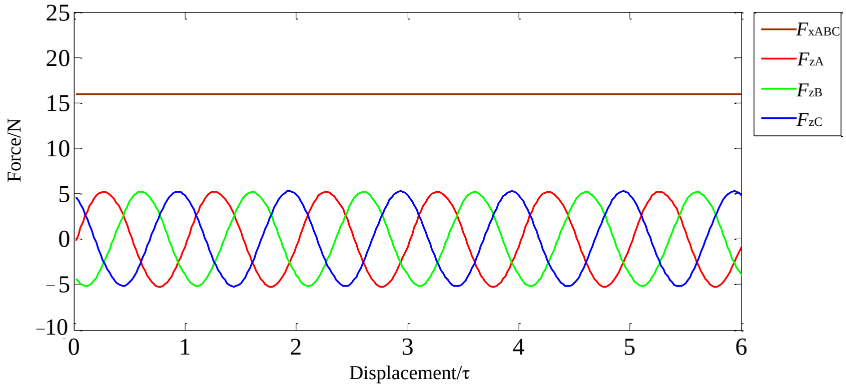

Figure 3. Horizontal resultant force and suspension force for each coil under q-axis current excitation (finite element simulation).

2.2. Analytical Model of Electromagnetic Force and Torque

To obtain the mathematical model of the relationship between electromagnetic force, torque, and current, it is necessary to first calculate the magnetic field generated by the permanent magnet array in the magnetic levitation linear motor. The magnetic field of the Halbach permanent magnet array is typically described using the fundamental harmonic model, as outlined in reference [22]. The fundamental harmonic model can be eventually solved as boundary-value problems using the Maxwell equation and the scalar potential [15,23].

To simplify the calculation, the following assumptions were made:

1. The relative magnetic permeability of the yoke is assumed to be infinite;
2. The magnet array has a periodicity over the horizontal and vertical direction, and the magnetization value of the permanent magnet is not changed;
3. The ending effect is neglected.

Figure 4 shows the magnetic field model of the permanent magnet array, which is a Halbach array structure. In Figure 4, two regions are defined: Region I represents air, and Region II represents the permanent magnet array. The boundary conditions are as follows.

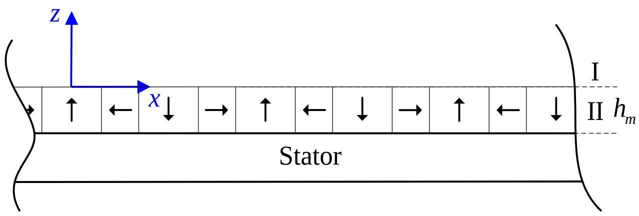

Figure 4. The magnetic field model of the permanent magnet array.

Given that the magnetic potential is zero at infinity, we can get the following equation:

$$\left.\frac{\partial A_{\mathrm{I}}}{\partial z}\right|_{z=\infty} = 0 \tag{1}$$

where A is the magnetic vector potential.

The magnetic permeability of the secondary yoke in a linear motor is assumed to be infinite, which means the magnetic potential in the corresponding region can be approximated as zero.

$$\left.\frac{\partial A_{\mathrm{II}}}{\partial z}\right|_{z=-h_{\mathrm{m}}} = 0 \tag{2}$$

where h_{m} is the thickness of the permanent magnet.

The continuity of the normal component of the magnetic induction vector $\boldsymbol{B}$ is maintained $B_{z\mathrm{I}} = B_{z\mathrm{II}}$:

$$\left.\frac{\partial A_{\mathrm{I}}}{\partial x}\right|_{z=0} = \left.\frac{\partial A_{\mathrm{II}}}{\partial x}\right|_{z=0} \tag{3}$$

Given $B_{x\mathrm{I}} = B_{x\mathrm{II}}$ at the interface, it can be known that

$$\left.\frac{\partial A_{\mathrm{I}}}{\partial z}\right|_{z=0} = \left.\frac{\partial A_{\mathrm{II}}}{\partial z}\right|_{z=0} \tag{4}$$

The magnetic flux density $\boldsymbol{B}$ can be decomposed in the x and z directions as follows [24]:

$$B_x(x,z) = -B_0 \mathrm{e}^{-\gamma z} \sin(\gamma x) \tag{5}$$

$$B_z(x,z) = B_0 \mathrm{e}^{-\gamma z} \cos(\gamma x) \tag{6}$$

$$B_0 = \frac{2\sqrt{2}\mu_0 M_0}{\pi}\left(1 - \mathrm{e}^{-\gamma h_m}\right) \tag{7}$$

where μ_0 and M_0 denote the permeability of the free space and the peak magnetization magnitude of permanent magnets, respectively. γ is the spatial wave number; $\gamma = \pi/\tau$.

The following assumptions are made while calculating the magnetic force and torque [25,26]:

1. The current in the conductor is evenly distributed;
2. There is no free charge in the studied field;
3. The coil and magnet arrays are rigid;
4. The coils are replaced by filament ones.

The Lorentz force equation method is the simplest approach for solving the electromagnetic model of ironless linear motors and planar motors. Reference [27] applied the Lorentz force equation method in the electromagnetic modeling of magnetic levitation permanent synchronous planar motors. Similarly, reference [25] used the Lorentz force equation method for the electromagnetic modeling of magnetic levitation permanent synchronous linear motors. The formula for calculating the coils in the permanent magnet array is given as follows [28]:

$$\boldsymbol{F} = \iiint_V \boldsymbol{J} \times \boldsymbol{B} \mathrm{d}V \tag{8}$$

$$\boldsymbol{T} = \iiint_V \boldsymbol{r} \times (\boldsymbol{J} \times \boldsymbol{B}) \mathrm{d}V \tag{9}$$

where $\boldsymbol{J}$ is the current density vector in the coil, V is the volume of the coil, and $\boldsymbol{r}$ is the force arm vector.

The $\boldsymbol{J}$ can be expressed as

$$\boldsymbol{J} = \begin{bmatrix} J_x & J_y & J_z \end{bmatrix}^{\mathrm{T}} \tag{10}$$

where J_x is the component on the x-axis, J_y is the component on the y-axis, J_z is the component on the z-axis.

By solving Equations (8) and (9), the electromagnetic force and torque generated by the j-th coil can be obtained:

$$F_{xj} = -2 l_c N K_z i_j B_0 \sin\left(\frac{\pi}{\tau}(x_j + p_x)\right) \tag{11}$$

$$F_{zj} = 2 l_c N K_z i_j B_0 \cos\left(\frac{\pi}{\tau}(x_j + p_x)\right) \tag{12}$$

$$T_{yj} = -2 l_c N K_z i_j B_0 \left(\cos\left(\frac{\pi}{\tau}(x_j + p_x)\right) x_j + \sin\left(\frac{\pi}{\tau}(x_j + p_x)\right) r_z\right) \tag{13}$$

$$K_z = \int_0^{h_c} e^{\left(-\frac{\pi}{\tau}(z+p_z)\right)} dz \tag{14}$$

where r_z represents the distance from the horizontal force to the center of the mover's mass. x_j represents the coordinate of the center of the coil in the mover's coordinate system. l_c represents the length of the coil along the y-direction. p_x and p_z are the relative position of the mover and stator.

In Equation (11), the term involving sin represents the variation of the magnetic field. During the control process, in order to introduce currents in a phase and at the same frequency, this term becomes the square of sin. Since the ABC three-phase windings correspond to magnetic field phases that are 120° electrical angles apart, the i_q current, after undergoing dq transformation, also results in three-phase currents with a sinusoidal variation pattern and phase differences of 120° electrical angles. The three sin squared terms, each differing by 120°, will always yield a constant value. When the three-phase windings move horizontally along the magnetic field, controlling the amplitude of the i_q current achieves control over thrust, and the same applies to the control of the levitation force.

The electromagnetic force generated in the horizontal direction by an MPMSLM can also generate a torque even if it is not transmitted through the mover. Figure 5 shows the force and force arm of an MPMSLM with the structure shown in Figure 1. In Figure 5, it can be seen that forces F_{z1} and F_{z2} produced by motor unit I and motor unit II, respectively, need to be combined to counterbalance the mass of the mover to maintain its levitation. To offset the additional torque, it is necessary to use the difference in forces F_{z1} and F_{z2} and the equivalent lever arm l_x to generate an opposite torque for balance. This torque is the product of the difference in forces F_{z1} and F_{z2} and the equivalent lever arm l_x. To generate a difference in forces F_{z1} and F_{z2}, it is necessary to control the difference between i_{d1} and i_{d2} currents. However, the sum of i_{d1} and i_{d2} currents must remain constant to maintain levitation. The greater the difference between i_{d1} and i_{d2} currents, the greater the difference in the three-phase currents of motor unit I and motor unit II, which requires the use of drivers with larger current ratings. Increasing the equivalent lever arm l_x can reduce the difference between i_{d1} and i_{d2}.

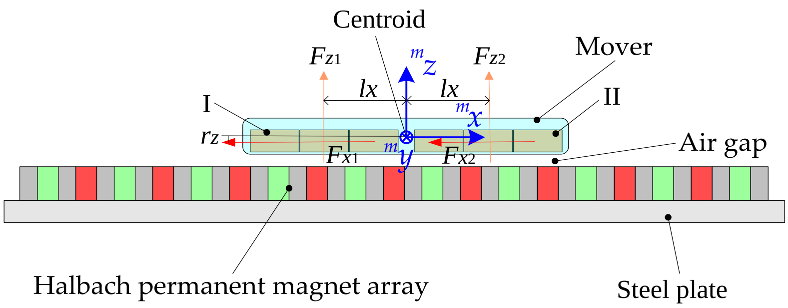

Figure 5. Schematic diagram of force and force arm of an MPMSLM.

3. Optimized Design of MPMSLM Structure

3.1. Optimized Design of Halbach Permanent Magnet Array

The goals of optimizing the permanent magnet array are twofold:

1. Optimizing the magnetic field to make it have better sinusoidal characteristics;
2. Increasing the electromagnetic force generated by the coil under the same coil size.

Increasing the thrust of the mover can improve the acceleration in motion control, while improving the sinusoidal characteristics of the air gap magnetic field can reduce the fluctuation of motor thrust and help decouple the suspension force and the horizontal force generated by the d-axis and q-axis currents. Therefore, in the motor design process, especially in the design of an MPMSLM, optimizing the parameters of the permanent magnet array is of great significance.

The Halbach array is a new type of permanent magnet arrangement that arranges magnets with different magnetization directions in a certain order, making the magnetic field significantly stronger on one side of the array and significantly weaker on the other side, and it is easy to obtain a magnetic field with an ideal sinusoidal distribution in space. These characteristics of the Halbach array have attracted the attention of numerous scholars and have been widely used in the field of linear motors [29–31].

Figure 6 shows the basic structure of the Halbach permanent magnet array. There are two types of magnets in Figure 6: an auxiliary magnet magnetized along the horizontal x-axis and a main magnet magnetized along the vertical z-axis. The Halbach structure in Figure 6 can enhance the magnetic field on the positive z-axis side. The size of the main and auxiliary magnets affects the distribution of magnetic induction intensity in the air gap, and thus the structure of the magnets needs to be optimized according to the desired performance indicators. When the pole pitch τ is a constant value, w_1, w_2, and h_m can affect the distribution of magnetic induction intensity in the air gap.

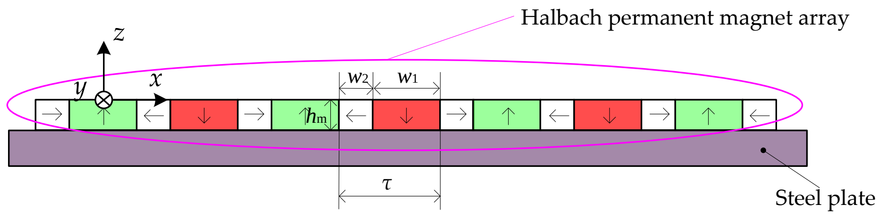

Figure 6. Halbach permanent magnet array and variable definition.

The variables w_1, w_2, and h_m in Figure 6 are set as design variables to optimize the thrust coefficient k_m of the linear motor. The pole pitch τ is set to 15, and the width of the main permanent magnet w_1 is set to 3 mm, 5 mm, 7 mm, 8 mm, 10 mm, and 12 mm, respectively. The width of the auxiliary permanent magnet w_2 is set to 12 mm, 10 mm, 8 mm, 7 mm, 5 mm, and 3 mm so that $w_1 + w_2 = \tau$. The thickness of the permanent magnet h_m is optimized within the range of 1 mm to 26 mm, with a point interval of 1 mm. Finite element simulation software is used to simulate and analyze the thrust coefficient k_m of the above variables under different size structures, and the simulation results are shown in Figure 7. k_m is the coefficient of interaction between B_0 in Equation (7) and the charged coils, which reflects the influence of permanent magnet size on the magnetic field in the final permanent magnet array.

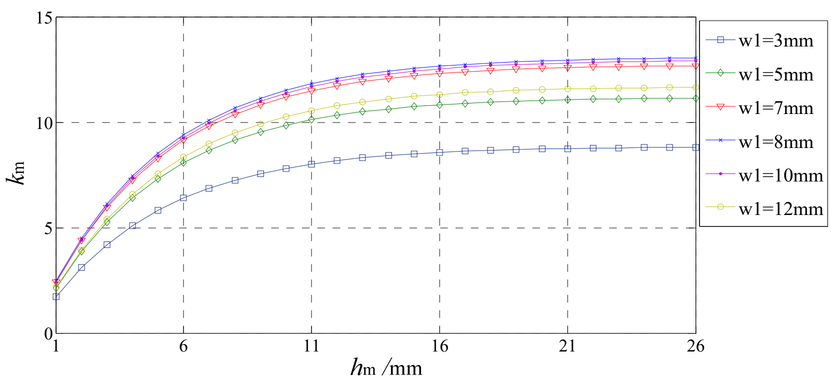

Figure 7. Variation curve of force coefficient k_m and permanent magnet size.

From Figure 7, it can be observed that the main magnet width w_1 and the auxiliary magnet width w_2 have the following effects on the thrust coefficient k_m: when w_1 = 3 mm, the coil generates a very small thrust. As w_1 increases, the thrust coefficient k_m increases until it reaches a critical point, after which k_m starts to decrease as w_1 continues to increase. Figure 7 shows that w_1 has a maximum value in the 8–10 mm range. Therefore, further finite element simulations were carried out in the 8–10 mm range with a step size of 0.1 mm. The main magnet width w_1 and auxiliary magnet width w_2 with the maximum thrust coefficient k_m were selected from the simulation results, with the values set as follows: w_1 = 8.7 mm and w_2 = 6.3 mm.

It can be observed from Figure 7 that the force coefficient changes greatly in the initial stage as the permanent magnet thickness h_m increases and then enters the saturation region. From Figure 7, we can also see that the trend of the force coefficient with the change in permanent magnet thickness is minimally affected by the width changes of the main and auxiliary permanent magnets. The permanent magnet thickness is selected as 20 mm.

3.2. Optimal Design of Coil Thickness

Increasing the thickness of the coil can make the winding have more turns and thus increase the output power of the motor. The magnetic field strength in the z-axis direction decays exponentially, and increasing the thickness of the coil increases the mass of the motor but has little effect on increasing the output power of the coil. Therefore, it is necessary to optimize the thickness of the coil. After determining the size of the permanent magnet, the thickness of the coil in the z-direction is simulated from 1–31 mm, with an increment of 1 mm, and the simulation results are shown in Figure 8.

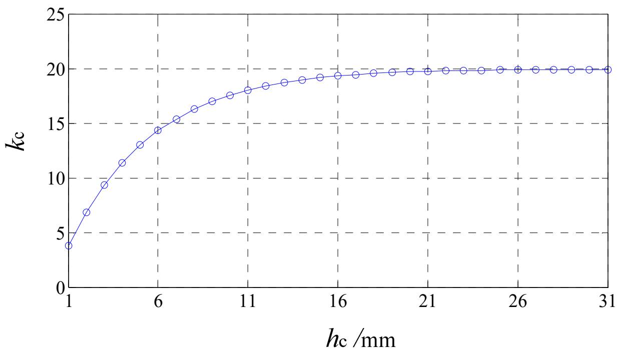

Figure 8. The relationship between coil thickness and force coefficient k_c.

In Figure 8, k_c denotes the influence of the coefficient of coil thickness on force. It is a comprehensive representation of Equations (7) and (14). It not only reflects the influence of coil size on electromagnetic force but also accounts for the impact of magnetic field attenuation in the z-direction on the force. It can be seen that in the initial stage of the curve, as the coil thickness increases, the electromagnetic force coefficient k_c increases significantly. However, when the coil thickness increases to 16 mm, the effect of further increasing the coil thickness on the coil output becomes very small due to the decay of the magnetic field. Therefore, considering all factors, a coil thickness of 15 mm is selected.

3.3. Design of Coil Topology

In order to reduce torque fluctuation and increase the effective length of the equivalent lever arm, a new MPMSLM structure is proposed in this paper, as shown in Figure 9. In Figure 9, the armature on the left side is composed of two sets of three-phase windings in series, which are powered by one set of driving units. The armature on the right side is composed of two sets of three-phase windings in series, which are 0.5 τ out of phase with the left-side winding, and the right-side winding is driven by one set of driving units. Therefore, this motor structure only uses two sets of driving units to achieve three-degrees-of-freedom motion control of the MPMSLM. The control input consists of four variables, namely the i_d and i_q currents of the left and right armature windings, and the output consists of two electromagnetic forces F_x and F_z and a torque T_y. By solving the four currents i_{d1}, i_{d2}, i_{q1}, and i_{q2}, the required electromagnetic forces F_x, F_z, and T_y can be obtained, thereby achieving the three-degrees-of-freedom control of the MPMSLM.

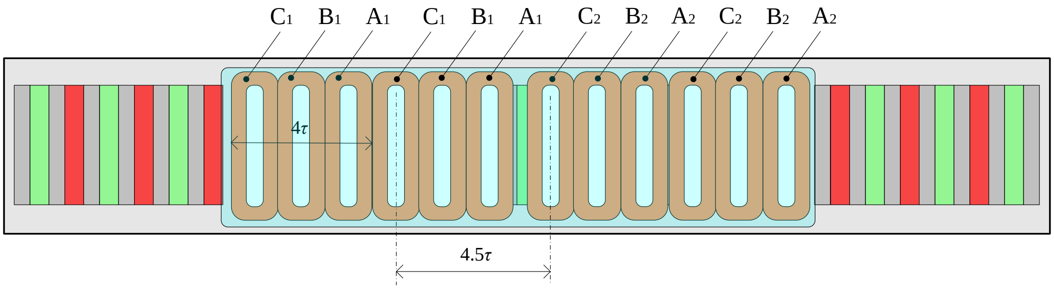

Figure 9. Motor structure proposed in this article.

3.4. Finite Element Simulation Analysis

To verify the above analysis, the torque and current of the MPMSLM are analyzed by finite element software. The ANSYS Electronics Desktop 2016.1 software is used for modeling and simulation, employing transient magnetic field simulation. The modeling process is as follows: Firstly, the specific structure of the motor is drawn in the software, and specific materials are assigned to each component as listed in Table 1. Next, an electric current excitation source is set up to simulate the flow of current in the windings. Subsequently, boundary conditions are defined for the finite element numerical calculation, which involves solving a matrix equation. The 'Balloon Boundary' condition is selected during the simulation process to reduce memory and CPU consumption, optimizing computational resources. Finally, motion settings are configured, with the mover (armature) set to move along the stator at a speed of 1.5 m/s. The two-dimensional model established during simulation did not take into account the inter-winding connection resistances and inductances. The overall dimensions of the simulation model are 800 mm × 60 mm × 100 mm, and the mesh size is set to 0.3 mm.

Table 1. Material allocation in simulation.

Components	Materials
Coil	Copper
Permanent magnet	NdFe36
Yoke plate	Steel_1010

In the simulation, the levitation force and horizontal thrust are kept constant, and the input current is solved through a decoupling matrix. The current was added to the system in an open-loop manner based on the relative position between the magnetic field and the mover. The structural data of the motor is shown in Table 2, and the mover's moving range is from 0 to 6 τ.

Table 2. Motor major parameters.

Parameters	Value	Unit
Pole pitch τ	15	mm
Air gap δ	1	mm
Winding size ($l_c \times w_c \times h_c$)	100 × 8 × 15	mm
Major permanent magnet size ($l_m \times w_1 \times h_m$)	100 × 8.7 × 20	mm
Auxiliary permanent magnet size ($l_m \times w_2 \times h_m$)	100 × 6.3 × 20	mm

Figure 10 presents the distribution of magnetic flux density obtained from finite element simulation. Figure 11 shows the variation curves of the magnetic flux density components B_z and B_x along the z and x axes at an air gap height of 6 mm. From Figure 11, it can be observed that both the magnetic flux density component B_z along the z-axis and the magnetic flux density component B_x along the x-axis exhibit good sinusoidal behavior. Higher sinusoidal behavior leads to smaller thrust fluctuations.

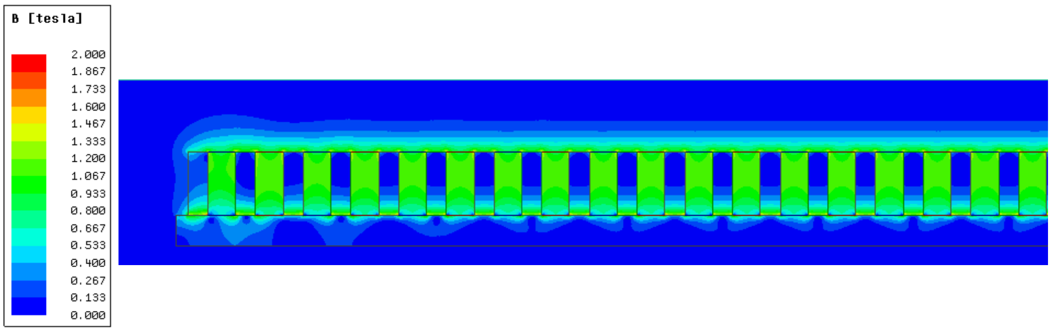

Figure 10. Magnetic flux density in the xz plane.

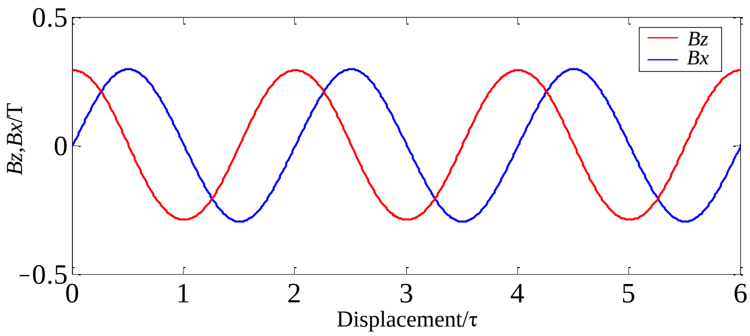

Figure 11. The variation curves of the magnetic flux density components B_z and B_x along the z and x axes at an air gap height of 6 mm.

It can be seen from Figure 12 that the decoupled electromagnetic force T_y can be maintained near 0, but there is also some fluctuation with position variation. The torque fluctuation range around the y-axis of the motor in this work (curve II) is -79.51 to 78.95 mN·m, while the T_y ripple range of the motor structure in Figure 1 (curve I) is -158.34 to 157.27 mN·m. It can be seen that the MPMSLM structure proposed in this paper has better open-loop decoupling performance than that of the MPMSLM in Figure 1.

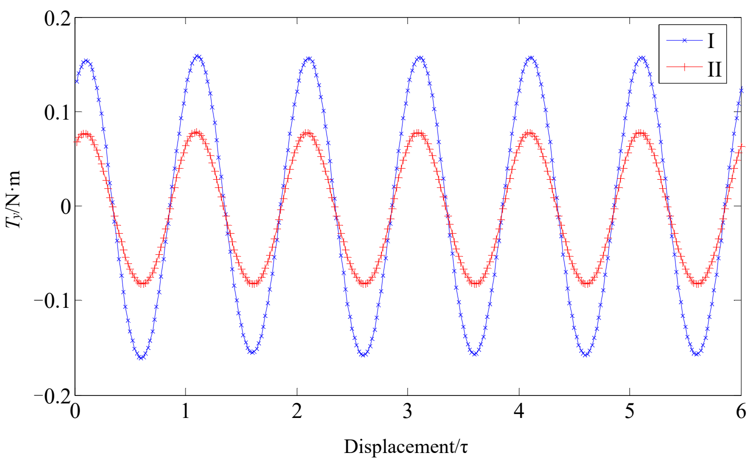

Figure 12. Torque T_y variation curve.

Figure 13 shows the input current waveforms of the MPMSLM proposed in this paper. It can be observed that the three-phase currents on the left side of the mover are larger than those on the right side during the operation of the motor. This is because the horizontal force does not generate a torque through the center of the mover and needs to be counteracted, which leads to the difference in the *d*-axis currents of the left and right winding units. Note that the *q*-axis currents of the two sets of windings are consistent during the operation.

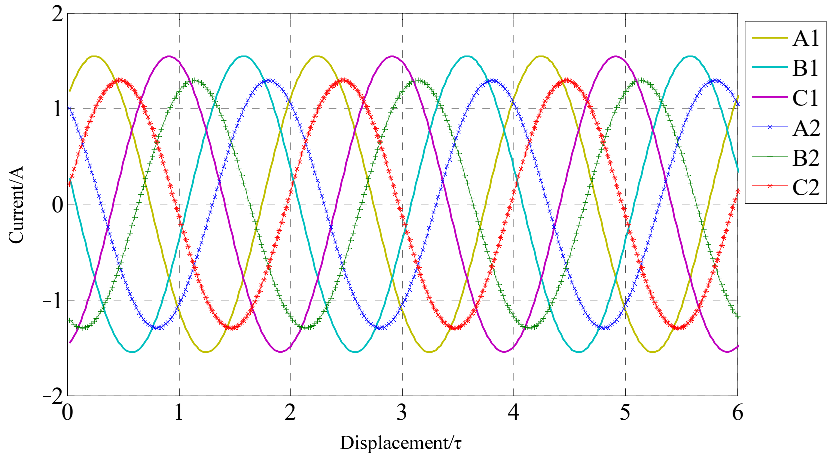

Figure 13. Current variation curve.

To compare and analyze the current distribution of the motor structure in Figure 1 and the MPMSLM structure proposed in this paper, the A-phase current of the two motor structures is selected for analysis. Since both the left and right sides of the mover in the MPMSLM structure proposed in this paper are composed of two sets of windings, the current for producing the same force is half that of the current in Figure 1. For a more intuitive comparison, the current in Figure 1 was halved. The current curves of the two motor structures are shown in Figure 14.

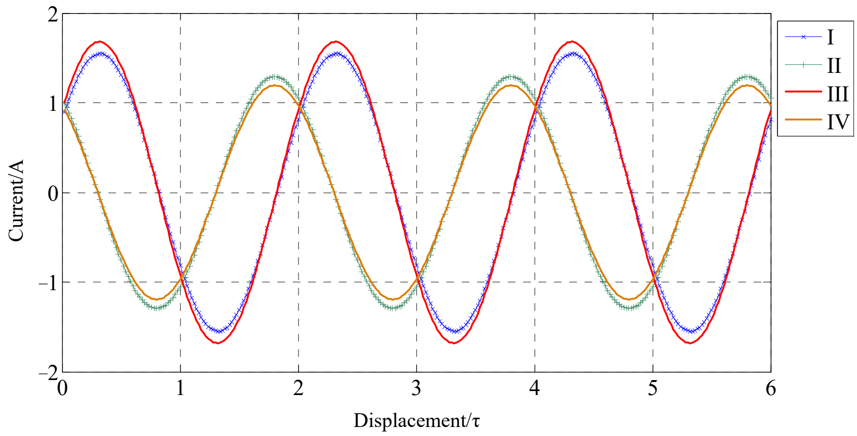

Figure 14. Comparison of current curves between two models.

In Figure 14, curves I and II are the current curves of the MPMSLM proposed in this paper, and the current range of the two-side windings is ±1.55 A and ±1.29 A, respectively. Curves III and IV in Figure 14 represent the current curves using the model in Figure 1, with a current range of ±1.68 and ±1.19, respectively. It can be seen that the proposed motor model in this paper has a small difference in current between the two-side windings when generating the same F_x and F_z, which can reduce the maximum current value of the driving unit. This is because our proposed structure has a longer effective force arm l_x from the coil to the center of mass.

Figure 15 shows the structural diagram of the 3D MPMSLM. It can be seen that the MPMSLM proposed in this work is composed of a mover and a stator, and the mover can achieve three-degrees-of-freedom motion above the stator. The mover includes a back plane and four sets of three-phase motor windings. The stator is composed of a yoke plate and Halbach permanent magnet array.

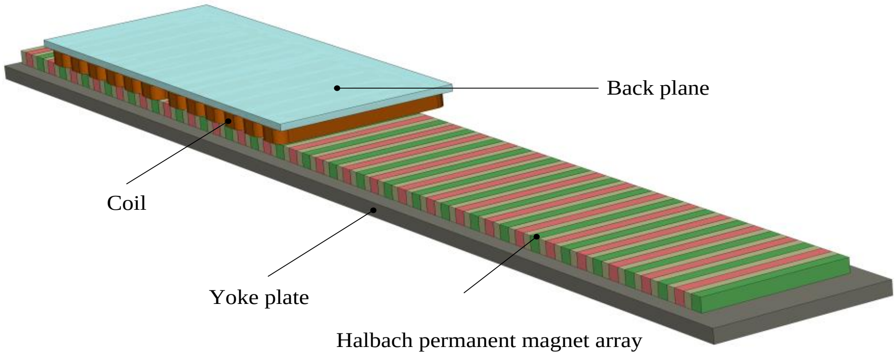

Figure 15. Basic structure of the proposed maglev linear motor.

4. Motion Control Analysis

4.1. Decoupling Design

The MPMSLM mover has no mechanical constraints during its motion. To achieve the levitation of the MPMSLM mover, it is necessary to control the electromagnetic forces and torques generated by the mover in three degrees of freedom. The electromagnetic thrust force F_x generated by the MPMSLM in Figure 5 can be expressed as

$$F_x = F_{x1} + F_{x2} = KK_z(i_{q1} + i_{q2}) \tag{15}$$

where K is the force coefficient related to the motor structure, and K_z is the term that reflects the influence of the mover's suspension height on force.

Similarly, the levitation force F_z can be written as

$$F_z = F_{z1} + F_{z1} = KK_z\ (i_{d1} + i_{d2}) \tag{16}$$

The torque in the mover coordinate system is given by

$$T_y = (F_{z1}\ - F_{z2})\ l_x = KK_z\ (i_{d1} - i_{d2})\ l_x \tag{17}$$

Equations (15)–(17) can be written as

$$\boldsymbol{W} = \begin{bmatrix} F_x & F_z & T_y \end{bmatrix}^{\mathrm{T}} \tag{18}$$

Based on the above-derived electromagnetic force and torque equation, the relation of them with the current can be expressed as

$$\boldsymbol{W} = \boldsymbol{K}(\boldsymbol{p})\boldsymbol{i} \tag{19}$$

$$\boldsymbol{i} = \begin{bmatrix} i_{q1} & i_{q2} & i_{d1} & i_{d2} \end{bmatrix}^{\mathrm{T}} \tag{20}$$

The matrix of $\boldsymbol{K}(p)$ is shown as

$$\boldsymbol{K}(\boldsymbol{p}) = \begin{bmatrix} KK_z & KK_z & 0 & 0 \\ 0 & 0 & KK_z & KK_z \\ 0 & 0 & KK_z\ l_x & -KK_z\ l_x \end{bmatrix} \tag{21}$$

The generalized inverse matrix of $\boldsymbol{K}(p)$ is shown as

$$\boldsymbol{K}^{-}(\boldsymbol{p}) = \boldsymbol{K}(\boldsymbol{p})^{\mathrm{T}}\left(\boldsymbol{K}(\boldsymbol{p})\boldsymbol{K}(\boldsymbol{p})^{\mathrm{T}}\right)^{-1} \tag{22}$$

Thus, we can derive the current in each winding as

$$\boldsymbol{i} = \boldsymbol{K}^{-}(\boldsymbol{p})\boldsymbol{W} \tag{23}$$

By using Equation (23), the two d-axis currents and two q-axis currents can be solved based on the desired electromagnetic force and torque, which enables the decoupling control of the MPMSLM.

The dynamic equation of the MPMSLM can be expressed as

$$\begin{cases} F_x = m\ddot{x} \\ F_z = m\ddot{z} + mg \\ T_y = I_y\ddot{\theta}_y \end{cases} \tag{24}$$

4.2. Structure of Control System

The closed-loop control of the MPMSLM aims to achieve closed-loop control of the three degrees of freedom of horizontal position x, suspension position z, and rotational angle θ around the y-axis, and its control system is shown in Figure 16. In Figure 16, x_r, z_r, and θ_r are the given values for the three degrees of freedom, while x, z, and θ are the actual values. The working principle is described as follows. First, the position deviation obtained from the comparison between the given value and the actual value is adjusted by the PID controller. The output of the PID is the required F_x, F_z, and T_y, which can be obtained through the decoupling module composed of Equation (23) to obtain the currents i_{d1}, i_{d2}, i_{q1}, and i_{q2}. The three-phase currents in each motor unit are calculated based on i_{d1}, i_{d2}, i_{q1}, and i_{q2}. Finally, the power amplification unit is used to drive the MPMSLM to achieve three-degrees-of-freedom motion control.

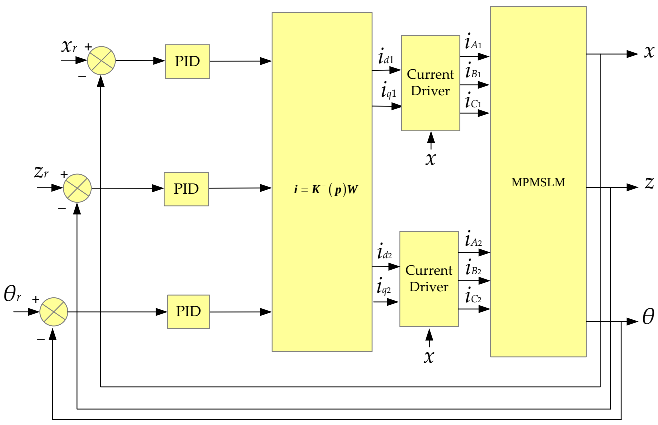

Figure 16. Control system structure.

4.3. Position Closed-Loop Control

The LabVIEW software was used to build the control system and verify and analyze the accuracy and robustness of the three-degree-of-freedom position closed-loop control.

Figure 17 shows the instability analysis of the position closed-loop system. It can be observed from Figure 17 that the system exhibits good stability.

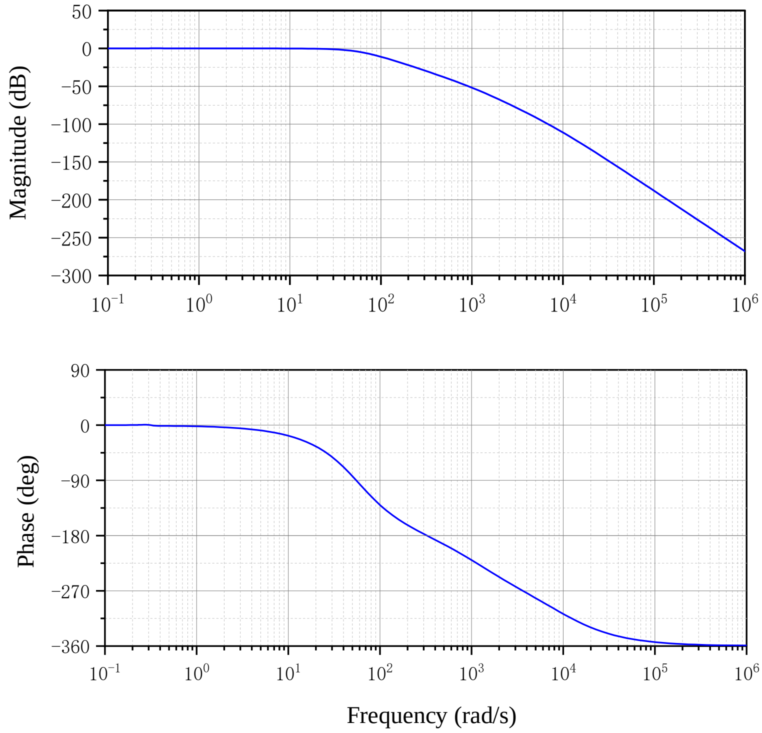

Figure 17. Position closed-loop Bode diagram.

Figure 18 shows the simulation model in the LabVIEW environment, where the program's running time is set to 1 ms. PID control is implemented using the built-in PID module in LabVIEW. The three PID controllers enable closed-loop control of the three degrees of freedom, allowing the control of the motion state of the MPMSLM based on the desired set points x_r, z_r, and θ_r. During the control process, the built-in PID controller of LabVIEW was employed. Except for the parameters K_c, T_i, and T_d, all other parameters were kept at their default values. The PID parameters for the three control degrees of freedom are shown in Table 3.

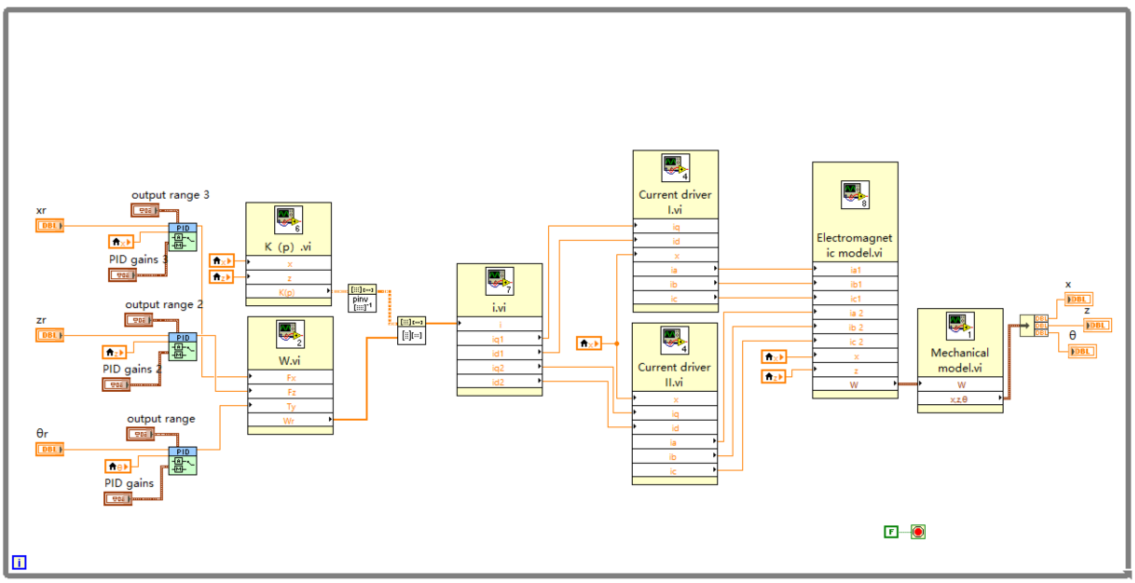

Figure 18. Simulation model in LabVIEW.

Table 3. The PID controller parameters for the three degrees of freedom.

Controller	K_c	T_i	T_d
x-axis controller	112	0.032	0.00008
z-axis controller	120	0.036	0.000075
θ-axis controller	352	0.008	0.00001

In Figure 18, the electromagnetic model and the mechanical model together form the model of the magnetic levitation permanent synchronous linear motor. In this setup, the inputs to the electromagnetic model are the electromagnetic forces F_x, F_z, and T_y generated by the current. The internal electromagnetic forces and torques F_{xj}, F_{zj}, and T_{yj} produced by each coil within the electromagnetic model are determined by Equations (11)–(13). The combined effect of these 12 coils results in the overall forces F_x, F_z, and T_y acting on the motor's mover. The mechanical model illustrates the conversion of forces and torques into displacements and angles. Forces F_x, F_z, and T_y, through Equation (24) (integrated once), yield velocities along the x-axis and z-axis and rotational velocity around the y-axis. Upon another integration, the resulting values provide displacements along the x-axis and z-axis, as well as angles of rotation around the y-axis.

During the simulation process, a step signal was added to the x-axis and z-axis to verify the three-degree-of-freedom position closed-loop performance of the MPMSLM. During the simulation, the z-axis position was 0, and at 0.1 s, it was stepped up to 1 mm. The given value of the x-axis position jumps from 0 mm to 100 mm at 0.6 s, and the rotation angle θ around the y-axis was set to 0.

The simulation results of the MPMSLM structure in Figure 1 are shown in Figure 19. In Figure 19a, we find that the angle θ generated on the y-axis ranges from −6.95 µrad to 5.23 µrad when the linear motor mover follows a step signal along the x-axis. Figure 19b shows the force and torque variation curves during the motion control process, where F_x ranges from −55.91 N to 149.82 N, F_z is the levitation force to counteract the weight of the mover, and T_y is the coupling torque generated on the y-axis when the x-axis follows the step signal, ranging from −2.85 N·m to 2.42 N·m.

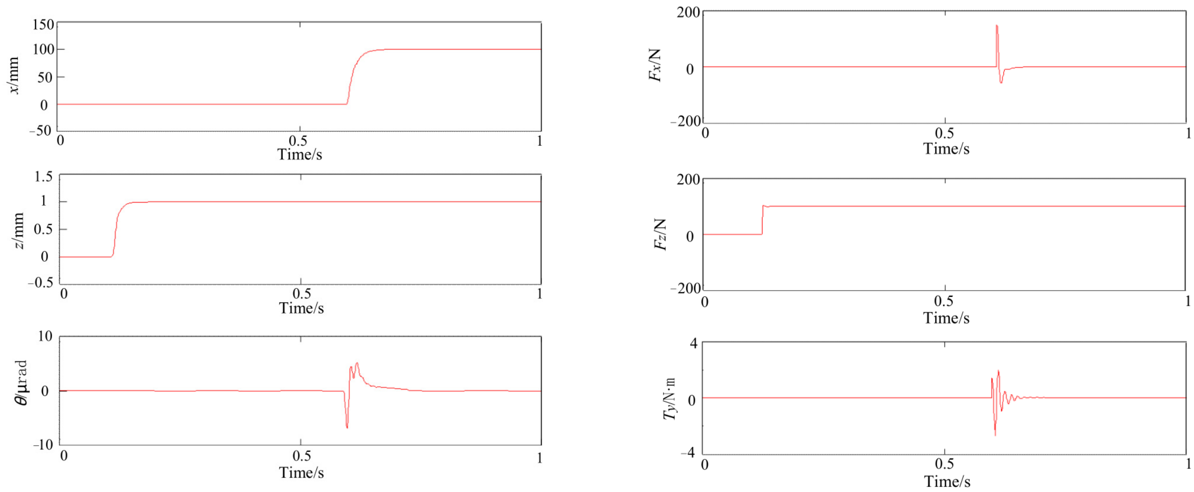

(**a**) (**b**)

Figure 19. Simulation results of motor structure motion control in Figure 1. (**a**) Displacement and rotation angle change curve. (**b**) Force and torque change curve.

The simulation results of the proposed model are shown in Figure 20, where the angle θ generated on the y-axis ranges from −3.89 µrad to 3.25 µrad, and T_y ranges from −2.09 N·m to 1.62 N·m when the x-axis follows the step signal. Through the above comparative analysis, it can be concluded that the MPMSLM structure proposed in this work has smaller torque fluctuations on the y-axis and hence smaller variations in θ when the MPMSLM performs closed-loop linear motion along the x-axis. Overall, the MPMSLM structure proposed in this paper has superior control performance.

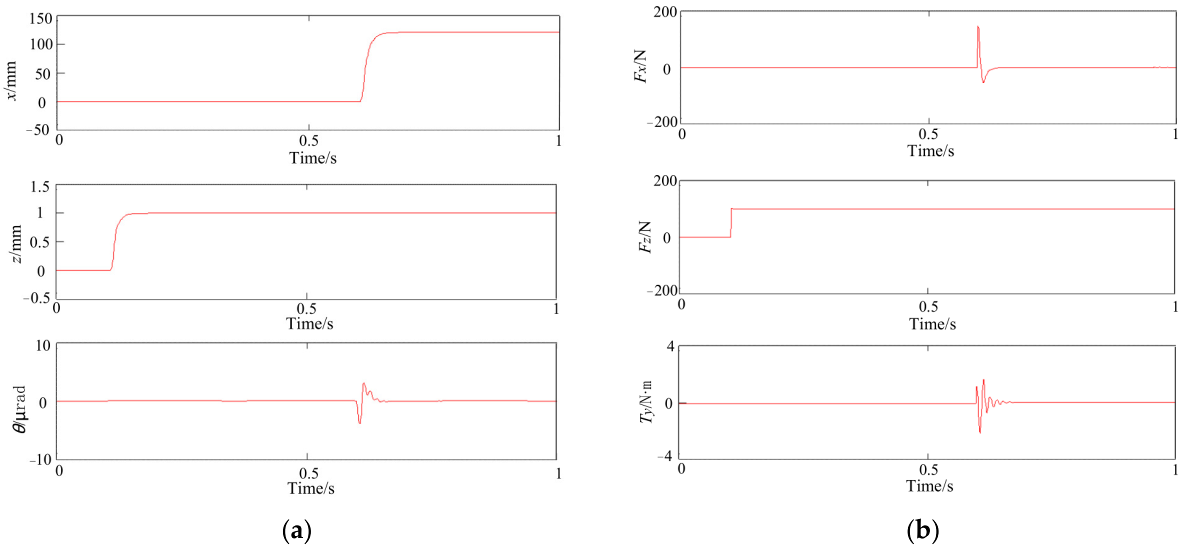

Figure 20. The simulation results of motor structure motion control proposed in this article. (**a**) Displacement and rotation angle curve. (**b**) Force and torque curve.

Figure 21 shows the current waveform during the closed-loop motion control process. Figure 21a shows the current waveform of the motor structure in Figure 1, while Figure 21b shows the current waveform of the motor structure proposed in this paper. By comparing the current waveforms of the two models, it can be concluded that the proposed motor structure has a smaller phase current. This is because the motor model has more coils and a longer equivalent lever arm l_x.

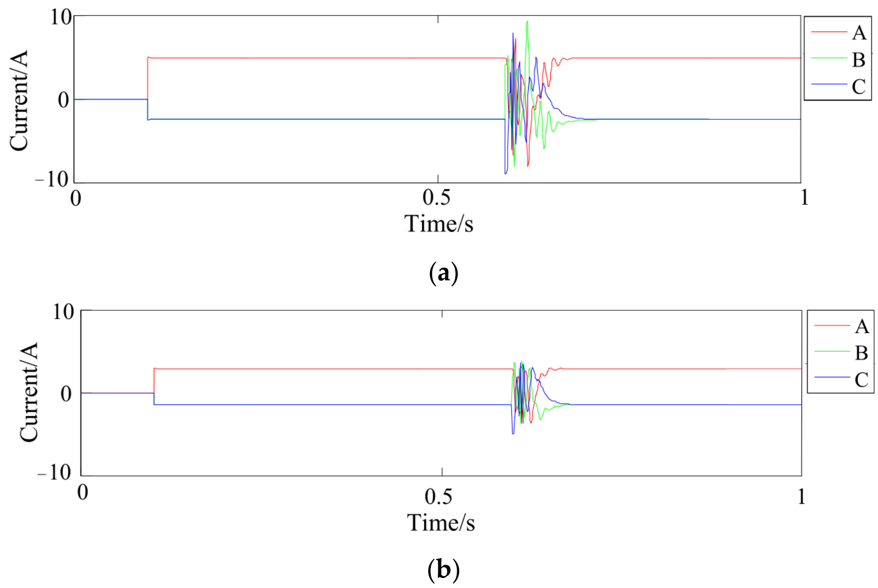

Figure 21. Current variation curve: (**a**) the current curve in the motor structure in Figure 1; (**b**) the current variation curve of the motor structure proposed in this article.

4.4. Result Analysis

Table 4 presents a comparative analysis of simulation data for θ and T_y. As F_x represents the active force generated by the x-axis motion, θ and T_y represent the passive fluctuations due to coupling during the x-axis motion. It is always desirable to have smaller fluctuations to achieve better performance. From Table 4, it can be observed that the proposed model in this paper exhibits smaller fluctuations in all parameters. In Table 4, it can be seen that the maximum ratio of θ and T_y fluctuations in the proposed model to those in the structure shown in Figure 1 is 1.79 and 1.49, respectively. This is due to the reduced coupling in the motor structure proposed in this paper, resulting in smaller additional torques during motion control.

Table 4. θ and T_y simulation data.

Parameters	Proposed Model (I)	Model in Figure 1 (II)	II/I
Positive direction θ	3.25 μrad	5.23 μrad	1.61
Negative direction θ	−3.89 μrad	−6.95 μrad	1.79
Positive direction T_y	1.62 N·m	2.42 N·m	1.49
Negative direction T_y	−2.09 N·m	−2.85 N·m	1.36

Table 5 provides data for the three-phase currents during the motion control process. For qualitative comparison, the maximum absolute value of each phase current was selected. Due to the use of an additional set of windings on both sides of the mover in the proposed model, only half of the current is required during the motion process. Additionally, the smaller structure coupling in Figure 1 results in smaller instantaneous current requirements. The use of smaller current supply helps reduce the working current of the driver's switching devices.

Table 5. Simulation data for three-phase currents.

Parameters	Proposed Model (I)	Model in Figure 1 (II)	II/I
$\lvert i_{\text{Amax}} \rvert$	3.55 A	7.96 A	2.24
$\lvert i_{\text{Bmax}} \rvert$	3.63 A	9.26 A	2.55
$\lvert i_{\text{Cmax}} \rvert$	4.85 A	8.87 A	1.83

5. Conclusions

This paper proposes a new MPMSLM structure that reduces the additional torque generated by using the dq transformation method for control through the design of the coil's topological structure. The traditional dq transformation and three-phase motor driver can be directly applied to the decoupling control of the MPMSLM, and this control scheme uses fewer switch devices to achieve the three-degree-of-freedom motion control of the MPMSLM. The finite element simulation results show that the proposed motor structure has smaller torque fluctuations and is more conducive to the decoupling control of the system. It also has a higher force coefficient under the same current drive with six sets of winding coils on each side of the moving part. Meanwhile, the rated current of the driving unit smaller can be smaller because a longer equivalent force arm can make the driving units on both sides of the moving part have a smaller current difference. Decoupling control of the motor was realized by using the method of generalized inverse matrix based on dq current transformation and electromagnetic modeling. The effectiveness of the proposed structure is verified in the LabVIEW software to have superior performance for three-degree-of-freedom position closed-loop control. Overall, our proposed architecture has better position closed-loop performance and smaller driving current.

Author Contributions: Conceptualization, F.X.; methodology, F.X.; software, F.X.; validation, Y.G.; formal analysis, C.Z.; investigation, X.S.; resources, C.Z.; data curation, Y.G.; writing—original draft preparation, F.X.; writing—review and editing, C.Z.; visualization, X.S.; supervision, C.Z.; project administration, C.Z.; funding acquisition, F.X. All authors have read and agreed to the published version of the manuscript.

Funding: This research was in part supported by the Scientific research funding project of the Liaoning Provincial Department of Education (JJL202015403), in part by the Shanghai Sailing Program (20YF1417000), and in part by a grant from Kyung Hee University (KHU-20222221).

Data Availability Statement: Not applicable.

Conflicts of Interest: The authors declare no conflict of interest.

References

1. Lu, M.H.; Cao, R.W. Comparative investigation of high temperature superconducting linear flux-switching motor and high temperature superconducting linear switched reluctance motor for urban railway transit. *IEEE Trans. Appl. Supercond.* **2021**, *31*, 3600605. [CrossRef]
2. Xu, L.; Sun, Z.M.; Zhao, W.X.; Liu, B.; Du, K.K.; Liu, G.H. Design and evaluation of linear primary permanent magnet vernier machines for urban railway transportation. *IEEE Trans. Ind. Appl.* **2023**, *59*, 1678–1688. [CrossRef]
3. Liu, Z.H.; Cai, C.G.; Lv, Q.; Yang, M. Improved control of linear motors for broadband transducer calibration. *IEEE Trans. Instrum. Meas.* **2021**, *70*, 1004910. [CrossRef]
4. Liu, Y.B.; Sun, W.C.; Buccella, C.; Cecati, C. Robust control of dual-linear-motor-driven gantry stage for coordinated contouring tasks based on feed velocity. *IEEE Trans. Ind. Electron.* **2023**, *70*, 6229–6238. [CrossRef]
5. Deng, C.; Ye, C.Y.; Yang, J.T.; Sun, S.J.; Yu, D.Z. A novel permanent magnet linear motor for the application of electromagnetic launch system. *IEEE Trans. Appl. Supercond.* **2020**, *30*, 4902005. [CrossRef]
6. Samimi, M.; Hassannia, A. Investigation of multi-layer secondary concept of an electromagnetic launcher. *IEEE Trans. Energy Convers.* **2022**, *37*, 921–926. [CrossRef]
7. Cao, R.W.; Cheng, M.; Zhang, B.F. Speed control of complementary and modular linear flux-switching permanent-magnet motor. *IEEE Trans. Ind. Electron.* **2015**, *62*, 4056–4064. [CrossRef]
8. Lu, Q.F.; Zhang, X.M.; Chen, Y.; Huang, X.Y.; Ye, Y.Y.; Zhu, Z.Q. Modeling and investigation of thermal characteristics of a water-cooled permanent-magnet linear motor. *IEEE Trans. Ind. Appl.* **2015**, *51*, 2086–2096. [CrossRef]
9. Xi, J.S.; Dong, Z.G.; Liu, P.K.; Ding, H. Modeling and identification of iron-less PMLSM end effects for reducing ultra-low-velocity fluctuations of ultra-precision air bearing linear motion stage. *Precis. Eng.* **2017**, *49*, 92–103. [CrossRef]
10. Mori, S.; Hoshino, T.; Obinata, G.; Ouchi, K. Air-bearing linear actuator for highly precise tracking. *IEEE Trans. Magn.* **2003**, *39*, 812–818. [CrossRef]
11. Lv, G.; Zhang, Z.X.; Liu, Y.Q.; Zhou, T. Analysis of forces in linear synchronous motor with propulsion, levitation and guidance for high-speed maglev. *IEEE J. Emerg. Sel. Top. Power Electron.* **2022**, *10*, 2903–2911. [CrossRef]
12. Lan, Y.P.; Li, J.; Zhang, F.G.; Zong, M. Fuzzy sliding mode control of magnetic levitation system of controllable excitation linear synchronous motor. *IEEE Trans. Ind. Appl.* **2020**, *56*, 5585–5592.
13. Wang, H.L.; Li, J.; Qu, R.H.; Lai, J.Q.; Huang, H.L.; Liu, H.K. Study on high efficiency permanent magnet linear synchronous motor for maglev. *IEEE Trans. Appl. Supercond.* **2018**, *28*, 0601005. [CrossRef]
14. Zhou, L.; Trumper, D.L. Magnetically levitated linear stage with linear bearingless slice hysteresis motors. *IEEE/ASME Trans. Mechatron.* **2021**, *26*, 1084–1094. [CrossRef]
15. Teo, T.J.; Zhu, H.Y.; Pang, C.K. Modeling of a Two degrees-of-freedom moving magnet linear motor for magnetically levitated positioners. *IEEE Trans. Magn.* **2014**, *50*, 8300512. [CrossRef]
16. Jansen, J.W.; van Lierop, C.M.M.; Lomonova, E.A.; Vandenput, A.J.A. Magnetically levitated planar actuator with moving magnets. *IEEE Trans. Ind. Appl.* **2008**, *44*, 1108–1115. [CrossRef]
17. van Lierop, C.M.M.; Jansen, J.W.; Damen, A.A.H.; Lomonova, E.A.; van den Bosch, P.P.J.; Vandenput, A.J.A. Model-based commutation of a long-stroke magnetically levitated linear actuator. *IEEE Trans. Ind. Appl.* **2009**, *45*, 1982–1990. [CrossRef]
18. Zhang, Y.M.; Ding, K.Z.; Du, S.S. Design study of a high loading superconducting magnetically levitated planar motor. *IEEE Trans. Appl. Supercond.* **2021**, *31*, 3601504. [CrossRef]
19. Overboom, T.T.; Smeets, J.P.C.; Jansen, J.W.; Lomonova, E. Torque decomposition and control in an iron core linear permanent magnet motor. In Proceedings of the 2012 IEEE Energy Conversion Congress and Exposition (ECCE), Raleigh, NC, USA, 15–20 September 2012; pp. 2662–2669.
20. van Lierop, C.M.M. Magnetically Levitated Planar Actuator with Moving Magnets: Dynamics, Commutation and Control Design. Ph.D. Thesis, Eindhoven University of Technology, Eindhoven, The Netherlands, November 2008.
21. Xing, F.; Kou, B.Q.; Zhang, L.; Wang, T.C.; Zhang, C.N. Analysis and design of a maglev permanent magnet synchronous linear motor to reduce additional torque in dq current control. *Energies* **2017**, *11*, 556. [CrossRef]
22. Kim, W.J. High-Precision Planar Magnetic Levitation. Ph.D. Thesis, Massachusetts Institute of Technology, Cambridge, MA, USA, June 1997.
23. Teo, T.J.; Chen, I.M.; Yang, G.; Lin, W. Magnetic field modeling of a dual-magnet configuration. *J. Appl. Phys.* **2007**, *102*, 074924. [CrossRef]
24. Zhu, H.Y.; Teo, T.J.; Pang, C.K. Design and modeling of a six-degree-of-freedom magnetically levitated positioner using square coils and 1-D Halbach arrays. *IEEE Trans. Ind. Electron.* **2017**, *64*, 440–450. [CrossRef]

25. Jansen, J.W.; Lomonova, E.A.; Vandenput, A.J.A.; van Lierop, C.M.M. Analytical model of a magnetically levitated linear actuator. In Proceedings of the Fourtieth IAS Annual Meeting. Conference Record of the 2005 Industry Applications Conference, Hong Kong, China, 2–6 October 2005; pp. 2107–2113.
26. Cao, J.C.; Deng, X.Q.; Li, D.; Jia, B. Electromagnetic analysis and optimization of high-speed maglev linear synchronous motor based on field-circuit coupling. *CES Trans. Elect. Mach. Syst.* **2022**, *6*, 118–123. [CrossRef]
27. Jansen, J.W. Magnetically Levitated Planar Actuator with Moving Magnets: Electromechanical Analysis and Design. Ph.D. Thesis, Eindhoven University of Technology, Eindhoven, The Netherlands, November 2007.
28. Zhang, S.G.; Niu, L.; Zhou, L.J.; Huang, J.T.; Hu, W.W.; Zhang, G.Q. Optimal matching design of length and width of rectangular ironless coils for magnetically levitated planar motors. *IEEE Access* **2019**, *7*, 185301–185309. [CrossRef]
29. Liao, Z.M.; Yue, J.G.; Lin, G.B. Application research of HTS linear motor based on Halbach array in high speed maglev system. *IEEE Trans. Appl. Supercond.* **2021**, *31*, 3600707. [CrossRef]
30. Shen, Y.M.; Lu, Q.F.; Li, Y.X. Design criterion and analysis of hybrid-excited vernier reluctance linear machine with slot Halbach PM arrays. *IEEE Trans. Ind. Electron.* **2023**, *70*, 5074–5084. [CrossRef]
31. Qin, W.; Ma, Y.H.; Lv, G.; Wang, F.Y.; Zhao, J.D. New levitation scheme with traveling magnetic electromagnetic Halbach array for EDS maglev system. *IEEE Trans. Magn.* **2022**, *58*, 8300106. [CrossRef]